Bayesian Inversion of Wrapped Satellite Interferometric Phase to Estimate Fault and Volcano Surface Ground Deformation Models

Yu Jiang[1] and Pablo J. González[1,2]

[1]COMET, Dept. Earth, Ocean and Ecological Sciences, School of Environmental Sciences, University of Liverpool, Liverpool, L69 3BX, United Kingdom

[2]Volcanology Research Group, Dept. Life and Earth Sciences, IPNA-CSIC, La Laguna, Tenerife, Spain

Key Points:

- We propose a new method to model the interferometric wrapped phase based on Bayesian inference and observations weighted by data covariance.
- An improved downsampling algorithm for wrapped interferometric phase is proposed for this, and we demonstrate its robustness.
- Our method extends geodetic modeling of InSAR data to cases where phase unwrapping is difficult or impossible, thus avoiding unwrapping errors.

Corresponding author: Yu Jiang, Yu.Jiang@liverpool.ac.uk

Corresponding author: Pablo J. González, pabloj.gonzalez@csic.es

Abstract

Bayesian inference and an improved downsampling method is used to determine earthquake and volcano source parameters using a popular geodetic observation method, satellite radar interferometry. The main novelty of the proposed approach is that the interferometric wrapped phase can be directly inverted, circumventing the ill-posed phase unwrapping processing step. Phase unwrapping errors severely affect the estimation of earthquake and volcano source parameters using interferometric observations, therefore it is desirable to avoid phase unwrapping completely. To overcome the need for phase unwrapping: we propose a downsampling algorithm and a method to estimate the covariance function of the wrapped phase, and establish an appropriate misfit function between the observed and simulated wrapped phase. Uncertainties in source parameters are assessed with a Bayesian approach, and finally the robustness of the inversion methodology is tested in multiple simulations including variable decorrelation and atmospheric noise simulations. The method is shown to be robust in challenging noise scenarios. It features an improvement in performance with the Bayesian approach, compared to similar previous methods, avoiding any influence of seed starting models, and escaping local minima. The impact of a small percentage of incorrectly unwrapped phase observations in current state-of-the-art methods is shown to strongly affect the estimation process. We conclude that in the cases where phase unwrapping is difficult or even impossible, the proposed inversion methodology with wrapped phase will provide an alternative approach to assess earthquake and volcano source model parameters.

1 Introduction

Phase unwrapping is the process of recovering the absolute phase from unambiguous wrapped phase values, measured in modulo 2π radians. The aim of phase unwrapping is to reconstruct the absolute value, because it is proportional to the difference in path length for a time-separated pair of SAR images. It provides a quantitative observation, which can be used to interpret ground deformation due to earthquake or volcanic processes, among others.

From a mathematical point of view, phase unwrapping is an inverse problem, however, it is ill-posed and notoriously difficult to solve in the presence of noise. The difference between the absolute phase and wrapped phase is an integer number of 2π radians, and the solution is non-unique unless further constraints are given. Although several assumptions have been made in the development of phase-unwrapping algorithms, a challenge still remains to overcome two common problems: noise and discontinuities in the absolute phase map (Werner et al., 2002; Huang et al., 2017). One constraining condition in such algorithms is a phase continuity assumption adopted by path-following algorithms, such as branch-cut (Goldstein et al., 1988), quality-guided (Xu & Cumming, 1996), or the minimum discontinuity approach (Flynn, 1997). Under this assumption, the absolute phase difference between any two neighboring pixels is assumed to be less than π. Various methodologies have been proposed to construct the path connecting pixels, to enable the absolute phases of all pixels to be determined through spatial or temporal integration. However, the phase continuity assumption is not satisfied everywhere, and it would be violated in the presence of high noise level or discontinuous terrain or surface displacements. High noise level could cause unwrapping errors, indeed an error at a single point will propagate into the rest of the unwrapped phase signal along the integration path. For areas where true discontinuities occur, the absolute difference between two adjacent pixels is more likely to be over π and the integration paths between those two pixels would not be allowed, so several disconnected regions would thus occur. Another popular constraining condition is to find the global minimum of an energy function based on the L^p norm of the difference between absolute phase differences and wrapped phase differences. When p=2, the L^p norm-based phase unwrapping method is transformed to the least squares phase unwrapping method, and when p=1, it is changed to the minimum-cost flow phase unwrapping method (Costantini, 1998; Chen & Zebker, 2001). The dilemma for solving the global minimization is that noisy pixels will distort

the solution, thus affecting the noise-free areas. Usually a phase filtering step is applied before unwrapping, however, phase information contained in noisy pixel areas can be lost.

Unwrapping error decreases the accuracy of geophysical models constrained using InSAR observations and their subsequent analysis (Huang et al., 2017; Whipple et al., 2016). One remedial measure is to correct the error after the unwrapping procedure. Some InSAR practitioners have attempted to manually correct unwrapping errors by adding integer multiples of 2π to badly unwrapped regions of pixels (Biggs et al., 2007), but it is a time-consuming process. Others designed an iterative unwrapping technique to identify and mitigate unwrapping errors, and this could reduce the number of pixels with unwrapping error to a lower level (Hussain et al., 2016). Ultimately however, unwrapping errors are difficult to mitigate and in some circumstance cannot be unambiguously detected.

A potential solution to avoid the unwrapping error issue completely is to carry out a geophysical inversion directly on the wrapped phase observations. A first pioneering approach to this was proposed a decade ago by creating an appropriate cost function based on the residual between observed and modeled wrapped phase (Feigl & Thurber, 2009). In their original work the authors directly used the observed wrapped phase, this was further refined in Ali and Feigl (2012), who used the downsampled phase gradient in range change (wrapped phase). In order to reduce the computation complexity, singular value decomposition (SVD) technique can be used during the nonlinear inversion (Fornaro et al., 2012). However, neither of the existing approaches considered estimating a variance-covariance matrix in their proposed cost function. Ignoring the observation correlations leads to inaccurate uncertainty bounds on the geophysical model parameters (Lohman & Simons, 2005). A second approach was to create a global network connecting the observed pixels, and calculate the difference in the observed wrapped phase between connected pixels (Hooper, 2010; Galetto et al., 2020; Wang et al., 2014). The cost function to minimize is the relationship between observed and modeled differential wrapped phase among connected pixels. The potential risk might be a huge matrix describing the relationship between connected pixels, which could cause numerical computation problems.

In this paper, we adopt the ideas of the first approach to minimizing the residual between observed and modeled wrapped phase, and also incorporating the wrapped phase gradients (Feigl & Thurber, 2009; Ali & Feigl, 2012). We propose an improved down-

sampling scheme for the wrapped phase and solve a variance-covariance matrix to evaluate the observations. Furthermore, the inverse problem is solved using state of the art techniques for geodetic source model inversions, accounting for full model uncertainties through a Bayesian approach (Anderson & Segall, 2013; González et al., 2015; Gombert et al., 2018; Ragon et al., 2018). Rather than providing only one set of optimal parameters (Maximum Likelihood Estimations), Bayesian approaches describe the optimum model as probability density function (PDF). They thus assess the model's uncertainties and have gained popularity recently as implemented in packages such as AlTar (Minson et al., 2013), BEAT (Vasyura-Bathke et al., 2017), GBIS (Bagnardi & Hooper, 2018), slipBERI (Amey et al., 2018).

The workflow of the manuscript is presented in Figure 1. We begin by providing the methodology to construct the likelihood function, including the new algorithm to downsample the wrapped phase, and a spectral method to estimate data correlation in the wrapped phase observations. A likelihood function suitable for Bayesian techniques is then derived. This is followed by a description of the sampling technique using a Markov Chain Monte Carlo (MCMC) method, which produces source models based on the classical Metropolis-Hasting (MH) rule. Finally, the proposed methodology is tested on synthetic cases with variable noise and one real earthquake case. We show that the performance of our proposed methodology is complementary and, under certain conditions, superior to the method using the unwrapped phase.

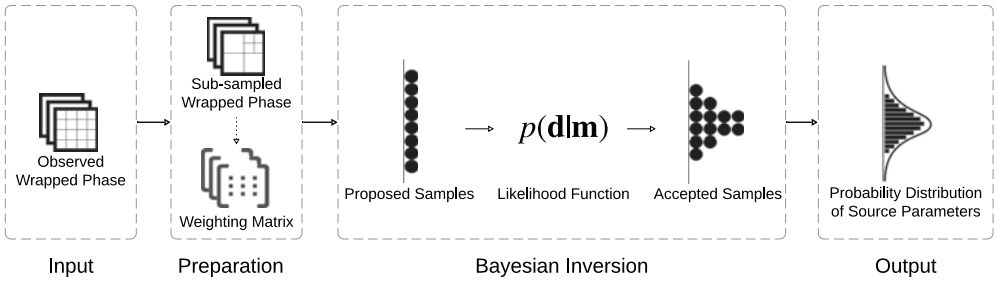

Figure 1. Schematic representation of the proposed inversion workflow with wrapped phase through a Bayesian approach. The input data are observed wrapped phase. Based on observations, the downsampled wrapped phase and its corresponding weighting matrix are prepared for constructing the likelihood function. Through a Bayesian approach, a series of samples are proposed and accepted according to the likelihood function. The accepted samples are then the posterior probability distribution of the source parameters.

2 Methodology: WGBIS

Solving a geophysical inverse problem must start with a clear understanding of the observed data, $\mathbf{d}$, and its relationship, $\mathbf{G}(\mathbf{m})$ with the model parameters $\mathbf{m}$. Such a relationship should also account for the existing of error sources, ϵ.

$$\mathbf{d} = \mathbf{G}(\mathbf{m}) + \epsilon \tag{1}$$

Bearing this framework in mind, we describe in this section how to treat the observed data, $\mathbf{d}$, referring to the downsampled wrapped phase and weighting scheme. Then we explain how to estimate the model parameters using a Bayesian approach built upon a state-of-the-art method, GBIS (Bagnardi & Hooper, 2018), hence the name WGBIS.

2.1 Data Downsampling and Weighting

Many downsampling algorithms have been developed for spatial downsampling and averaging of interferograms. The number of data points, as well as the noise, is reduced while as much information as possible is retained (Jonsson et al., 2002; Simons et al., 2002; Lohman & Simons, 2005). Most although not all downsampling algorithms recursively divide the data into quads, until the variance of the data within each smaller quad is below a preset threshold. Feigl and Sobol (2013) extended the quadtree downsampling approach to the wrapped phase. However, their approach estimates the gradient of range change by averaging the difference between rows or columns, which could be sensitive to the noise on the edge of the patch. We propose a modification that takes advantage of the redundancy of data within each patch, by using robust fitting of a bi-linear ramp. Our experiments show that an iterative fitting method is more robust against noise than a least-square algorithm. We also remove such trends to obtain an unbiased estimate of the variance of the wrapped phase data.

2.1.1 Data Downsampling

Our proposed methodology to downsample the wrapped phase, φ, is to subdivide the phase map recursively into patches for which we estimate: (1) a circular mean phase value, $\overline{\varphi}$, (2) an estimate of the discrete spatial derivative of range change with respect to the East-coordinate (or X-direction), ψ_X, and (3) an estimate of the discrete spatial derivative of range change with respect to the North-coordinate (or Y-direction), ψ_Y.

It is assumed that a given patch of size n pixels contains wrapped phase values $\varphi(i,j)$, where i and j are the indexes in the X- and Y-direction. Note that the following equations are valid for circular statistics (Mardia & Jupp, 2000). For each patch and at each iteration, the procedure is as follows:

(1) To estimate the circular mean phase of the patch, $\overline{\varphi}$,

$$\begin{aligned}\overline{C_\varphi} &= \frac{1}{n^2}\sum_{i=1}^{n}\sum_{j=1}^{n}\cos\varphi(i,j)\\ \overline{S_\varphi} &= \frac{1}{n^2}\sum_{i=1}^{n}\sum_{j=1}^{n}\sin\varphi(i,j)\\ \overline{\varphi} &= \arctan(\frac{\overline{S_\varphi}}{\overline{C_\varphi}}) + \frac{\pi}{2}(1+\frac{\overline{C_\varphi}}{|\overline{C_\varphi}|})\end{aligned} \tag{2}$$

(2) The range change gradients ψ_X and ψ_Y are calculated in X- and Y-directions. The phase in space domain is projected into the spectral domain with a 1-dimension Fourier Transform in X- and Y-directions, separately. We take advantage of the observation that the power of specific wavenumbers corresponds to the number of fringes in the space domain. Using this approach, it can be empirically determined if a given patch has less than one fringe. Hence, there should be less than two dominant frequencies with high power in both X- and Y-directions, and a robust linear regression algorithm, "robustfit", is directly used for the wrapped phase to estimate the gradients. A more rigorous approach is possible but this straightforward method performs well. We define a frequency to be of high power, $P_X(f_X)$ or $P_Y(f_Y)$, if the power spectrum is higher than three standard deviations from the mean power spectrum.

$$\begin{aligned}P_X(f_X) &> \mu(P_X) + 3\sigma(P_X)\\ P_Y(f_Y) &> \mu(P_Y) + 3\sigma(P_Y)\end{aligned} \tag{3}$$

where $\mu(P_X)$ and $\mu(P_Y)$ are the mean power spectra, and $\sigma(P_X)$ and $\sigma(P_Y)$ are their standard deviations. For the patch having no more than one frequency with high power in both X- and Y-directions, a bi-linear function is applied to fit the phase and estimate the gradient.

$$\hat{\varphi} = \overline{\varphi} + \Delta X\psi_X + \Delta Y\psi_Y \tag{4}$$

where ΔX and ΔY are the coordinates with respect to the center of the patch.

(3) Following Feigl and Sobol (2013) and Ali and Feigl (2012) we estimate the wrapped phase mean deviations. First, the circular mean deviation, σ_1, is calculated.

$$\sigma_1 = \frac{1}{n^2}\sum_{i=1}^{n}\sum_{j=1}^{n}\{\pi - |\pi - |\varphi(i,j) - \overline{\varphi}||\} \tag{5}$$

Secondly, we remove the ramp from the phase and calculate the circular mean deviation, σ_2, of the de-ramped phase (Nikolaidis & Pitas, 1998).

$$\overline{\varphi}' = \frac{1}{n^2}\sum_{i=1}^{n}\sum_{j=1}^{n}\{\varphi(i,j) - (\overline{\varphi} + \Delta X\psi_X + \Delta Y\psi_Y)\}$$
$$\sigma_2 = \frac{1}{n^2}\sum_{i=1}^{n}\sum_{j=1}^{n}\{\pi - |\pi - |\varphi(i,j) - \overline{\varphi}'||\} \tag{6}$$

Different criteria were studied for downsampling circular mean phase and gradient of range change. We concluded that for any given quad, the following conditions must be checked, if any of them are met the quad is sub-divided and then steps (1) to (3) are again calculated in the child quads: a) if there is more than one wavenumber with high power, as defined in step (2) along X- or Y-direction; b) if the circular mean deviation of phase is higher than a predefined maximum threshold for circular mean deviation, $\sigma_1 > \sigma_{1,crit}$; and c) if the circular mean deviation of the de-ramped phase exceeds a second predefined maximum threshold of circular mean deviation, $\sigma_2 > \sigma_{2,crit}$. Ultimately, the iteration is forced to stop if the number of pixels within the current patch is less than a given minimum pixel threshold, $n^2 \leq n^2_{thresh}$.

The initial inspiring sub-dividing methodology for wrapped phase, PHA2QLS.C (Feigl & Sobol, 2013), estimates the phase gradient by averaging the gradient between consecutive pixels in rows (or columns) within each patch. We noted that this approach can be sensitive to phase noise on the edge of the patch. Therefore, the performance in the estimation of phase gradients was compared between a) the PHA2QLS algorithm, b) a simple least squares bi-linear ramp method, and c) a bi-linear ramp fitted using a robust iterative least-squares method. Our experiments show that the robust fitting method provides a significant improvement against noise in the estimation of the gradients, with only a modest increase in computation time.

2.1.2 Data Weighting

Accounting for all noise sources in satellite radar interferograms is complex (González & Fernández, 2011), but essential to accurately estimate geophysical model parameters (Lohman & Simons, 2005). Here, we focus on the characterization of the spatial pattern

of noise. This involves estimating the data variance-covariance matrix, C, to enable calculating a data weighting matrix, W.

$$W = C^{-1} \tag{7}$$

We start with the gradient of range change, ψ, this being relatively easier as it is a continuous differentiable field (Sandwell & Price, 1998). Therefore, we are able to calculate the corresponding covariance function directly using popular geostatistical methods. Adopting the semi-variogram, first an empirical semi-variogram is first estimated and then a theoretical semi-variogram model fitted to the estimated empirical observations. The general idea is to exploit the correlation of values of pairs of pixels, a closer pair is more similar than those farther apart, so the spatial decay of the correlation provides useful information on the noise characteristics. We search for pixel pairs with a given distance Δh_i, and calculate the variance $\gamma(\Delta h_i)$.

$$\gamma(\Delta h_i) = \frac{\sum \left[\psi^j - \psi^k\right]^2}{2M} \tag{8}$$

where M is the number of pixel pairs with the distance Δh_i. The series of Δh_i and $\gamma(\Delta h_i)$ are used to estimate the semi-variogram parameters.

$$\hat{\gamma}(\Delta h_i) = n_\psi + (s_\psi - n_\psi)\big(1 - exp\big(-\frac{\Delta h_i}{h_\psi}\big)\big) \tag{9}$$

where n_ψ is the nugget variance, s_ψ is the sill variance, and h_ψ is the range. Three semi-variogram parameters are then used to construct its covariance function, and the covariance value between two pixels with distance h is $\rho_\psi(h)$.

$$\rho_\psi(h) = n_\psi + (s_\psi - n_\psi)exp\big(-\frac{h}{h_\psi}\big) \tag{10}$$

For circular mean phase, the circular mean deviation of the de-ramped phase, σ_2, described the noise level within each patch, so we make use of the square of the circular mean deviation, σ_2^2, as the diagonal term of the variance-covariance matrix. However, the circular mean phase is a spatially discontinuous function, and we are not able to evaluate the characteristics of the spatially correlated noise directly, therefore we ignore the correlation of circular mean phase between patches.

2.2 Bayesian Parameters Estimation

In this section, we present the methodology in detail, as shown in Figure 2.

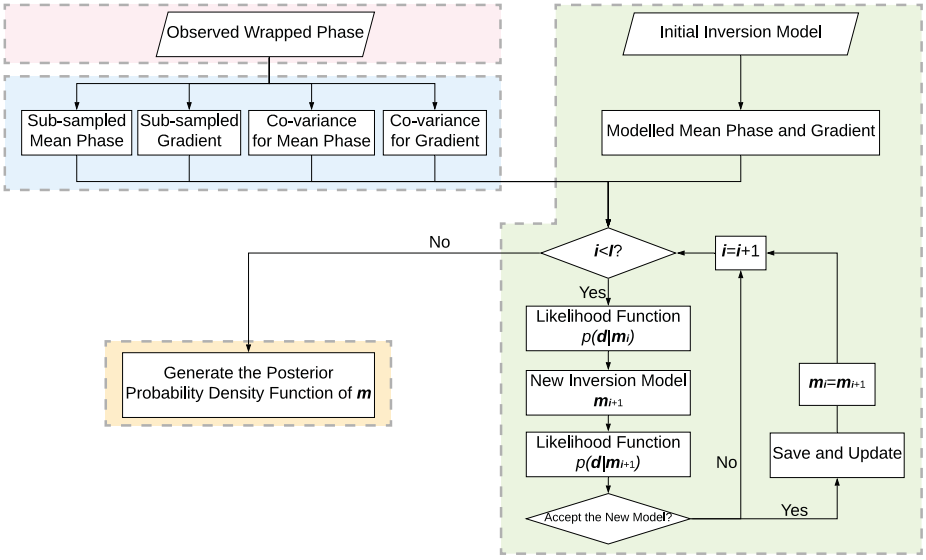

Figure 2. Framework of the proposed methodology, WGBIS. This figure is a detailed illustration of the schematic representation in Figure 1, pink box: Input, blue box: Preparation, green box: Bayesian Inversion, orange box: Output. The input data is the observed wrapped phase. For data preparation, the observation wrapped phase is reduced to downsampled mean phase and phase gradient with the quadtree algorithm described in section 2.1.1. The variance-covariance matrix for data weighting is calculated for circular mean phase and phase gradient respectively in section 2.1.2. For Bayesian inversion in the green box, the likelihood function is calculated from the downsampled wrapped phase and variance-covariance matrix, which is explained in section 2.2. According to the Monte Carlo Markov Chain algorithm, the new inversion model $\boldsymbol{m}_{i+1}$ is randomly generated, based on its previous model, $\boldsymbol{m}_i$. the Metropolis-Hasting rule is applied to decide whether to accept or further update the new model on the basis of the likelihood function. The posterior probability density function of the model is the collection of accepted models after the Bayesian inversion.

2.2.1 Bayesian Framework

In the Bayesian framework, the unknown model parameters are described by probability density function (PDF), which is updated after adding the new information source.

Prior information on model parameters is named a prior PDF. After adding more information provided by likelihood function, $p(\mathbf{d}|\mathbf{m})$, the Bayesian approach updates the prior PDF, $p(\mathbf{m})$, to posterior PDF, $p(\mathbf{m}|\mathbf{d})$, as described in equation 11.

$$p(\mathbf{m}|\mathbf{d}) = \frac{p(\mathbf{d}|\mathbf{m})p(\mathbf{m})}{p(\mathbf{d})} \tag{11}$$

where $p(\mathbf{d}|\mathbf{m})$ is the likelihood function based on residuals between the observed data $\mathbf{d}$ and the model predictions $\mathbf{G}(\mathbf{m})$, and $p(\mathbf{d})$ is a constant number independent of $\mathbf{m}$. In this methodology, the prior PDF, $p(\mathbf{m})$, is assumed to be a uniform distribution with the lower and upper bounds based on our previous knowledge, and it means the probability value is the same for all the trial models. This assumption is reasonable, especially for the blind fault we had never previously studied. Thus, we will later focus on the likelihood function, since the posterior PDF, $p(\mathbf{m}|\mathbf{d})$, is proportional to the likelihood function, $p(\mathbf{d}|\mathbf{m})$, and they share a similar PDF.

$$p(\mathbf{m}|\mathbf{d}) \propto p(\mathbf{d}|\mathbf{m}) \tag{12}$$

For consistency in the statistical treatment of the unbounded phase gradients, we approximate the phase as a wrapped normal distribution, instead of the von Mises distribution used in Feigl and Thurber (2009). The wrapped normal distribution and the von Mises distributions are important in the analysis of circular data, and they are similar in some ways (Kent, 1978): the von Mises distribution converges towards the wrapped normal distribution when its concentration parameter (κ) tends towards infinity (Pepe, 2019). The convolution of two wrapped normal variables is also wrapped normal (Jammalamadaka & SenGupta, 2001), but the multivariate von Mises distribution requires a rather complex estimation procedure (Mardia & Voss, 2014). The maximum likelihood parameter estimation in multivariate von Mises is also still an open problem (Nodehi et al., 2018). Assuming the error ϵ in equation 1 follows the multivariate wrapped normal distribution with zero mean and variance-covariance matrix $\mathbf{C}$, the likelihood function $p(\mathbf{d}|\mathbf{m})$ is as expressed in equation 13.

$$\begin{aligned} p(\mathbf{d}|\mathbf{m}) &= (2\pi)^{-\frac{N}{2}}|\mathbf{C}|^{-\frac{1}{2}}exp\big[-\frac{1}{2}\mathbf{r}^T\mathbf{C}^{-1}\mathbf{r}\big] \\ \mathbf{r} &= \mathbf{G}(\mathbf{m}) - \mathbf{d} - 2\pi k \end{aligned} \tag{13}$$

where $\mathbf{r}$ is the residual between the model predictions $\mathbf{G}(\mathbf{m})$ and the observed data $\mathbf{d}$, N is the number of data points, and i is an integer. Using the wrapped normal distribution is ambiguous to the integer k, however in our specific case the spatial distribution of the InSAR phase values permits discarding ambiguous models during the Bayesian estimation. In addition, the observed phase gradient is also incorporated in the inversion, and phase gradient is very sensitive to the integer k: an incorrect estimate of k would severely affect the observed phase gradient and dramatically increase the residual.

After phase downsampling, we will have three downsampled data sets (circular mean phase and phase gradients), and we combine three observation sets in the inversion as equation 14 shows.

$$
\begin{aligned}
p(\mathbf{d}|\mathbf{m}) &= (2\pi)^{-\frac{\sum N}{2}} |\mathbf{C}|^{-\frac{1}{2}} exp\big[-\frac{1}{2}\mathbf{r}^T\mathbf{C}^{-1}\mathbf{r}\big] \\
\mathbf{r} &= \begin{bmatrix} \mathbf{r}_1 \\ \mathbf{r}_2 \\ \mathbf{r}_3 \end{bmatrix} \\
\mathbf{C} &= \begin{bmatrix} \mathbf{C}_1 & 0 & 0 \\ 0 & \mathbf{C}_2 & 0 \\ 0 & 0 & \mathbf{C}_3 \end{bmatrix}
\end{aligned} \tag{14}
$$

For the variance-covariance matrix $\mathbf{C}$ in equation 14, if neglecting the correlation between observations sets, then $\mathbf{C}$ is a diagonal variance-covariance and thus $\mathbf{C}_1$, $\mathbf{C}_2$ and $\mathbf{C}_3$ are each diagonal. If one instead considers the spatial correlation between patches, but neglects the correlation within an individual patch, then $\mathbf{C}$ becomes a block-diagonal matrix with $\mathbf{C}_1$ diagonal but $\mathbf{C}_2$ and $\mathbf{C}_3$ full.

For circular mean phase, the residual phase $\mathbf{r}_1$ is the wrapped difference of the observed and modelled circular mean phase, $\mathbf{r}_1 = wrap(\mathbf{G}_1(\mathbf{m}), \mathbf{d}_1)$. Note that the $wrap(.)$ operator is not a linear operator because $wrap(a-b) \neq wrap(a) - wrap(b)$. The residual phase of circular mean phase can be calculated in MatLab as equation 15 (Feigl & Thurber, 2009).

$$
\mathbf{r}_1 = angle\big\{complex\big[\cos(\mathbf{G}_1(\mathbf{m}) - \mathbf{d}_1), \sin(\mathbf{G}_1(\mathbf{m}) - \mathbf{d}_1)\big]\big\} \tag{15}
$$

The modeled circular mean phase $\mathbf{G}_1(\mathbf{m})$ is the absolute phase in line-of-sight direction.

$$\begin{aligned} \mathbf{G}_1(\mathbf{m}) &= \mathbf{s} \cdot \mathbf{u} \cdot c \\ \mathbf{u} &= [\mathbf{u}_E \quad \mathbf{u}_N \quad \mathbf{u}_U]^T \\ \mathbf{s} &= [-\cos(\alpha')\sin(\theta) \quad \sin(\alpha')\sin(\theta) \quad \cos(\theta)] \\ c &= \frac{-4\pi}{\lambda} \end{aligned} \tag{16}$$

where $\mathbf{u}$ is the modeled 3-component displacement vector. Generally $\mathbf{s}$ is the unit vector for projecting the observation vector from Cartesian coordinates to line-of-sight direction with incidence angle θ, and angle $\alpha' = \alpha + \beta$ is the combined effect of heading, α, and, β, squint angles (González et al., 2015), and c is the constant value for converting units from meters to radians with radar microwave wavelength λ.

For the gradient of range change, the residuals $\mathbf{r}_2$ and $\mathbf{r}_3$ are calculated in equation 17.

$$\begin{aligned} \mathbf{r}_2 &= \mathbf{G}_2(\mathbf{m}) - \mathbf{d}_2 \\ \mathbf{r}_3 &= \mathbf{G}_3(\mathbf{m}) - \mathbf{d}_3 \end{aligned} \tag{17}$$

Note that the unit is radians/meter for $\mathbf{G}_2(\mathbf{m})$, $\mathbf{G}_3(\mathbf{m})$, $\mathbf{d}_2$, $\mathbf{d}_3$. The modeled gradient of range change in X-direction, $\mathbf{G}_2(\mathbf{m})$, and in Y-direction, $\mathbf{G}_3(\mathbf{m})$ is the projection of the East- and North-components of phase gradient into the line-of-sight direction.

$$\begin{aligned} \mathbf{G}_2(\mathbf{m}) &= \mathbf{s} \cdot \frac{\partial \mathbf{u}}{\partial x} \cdot c \\ \frac{\partial \mathbf{u}}{\partial x} &= [\frac{\partial \mathbf{u}_E}{\partial x} \quad \frac{\partial \mathbf{u}_N}{\partial x} \quad \frac{\partial \mathbf{u}_U}{\partial x}]^T \\ \mathbf{G}_3(\mathbf{m}) &= \mathbf{s} \cdot \frac{\partial \mathbf{u}}{\partial y} \cdot c \\ \frac{\partial \mathbf{u}}{\partial y} &= [\frac{\partial \mathbf{u}_E}{\partial y} \quad \frac{\partial \mathbf{u}_N}{\partial y} \quad \frac{\partial \mathbf{u}_U}{\partial y}]^T \end{aligned} \tag{18}$$

where $\frac{\partial \mathbf{u}}{\partial x}$ is the displacement gradient in X-direction, and $\frac{\partial \mathbf{u}}{\partial y}$ is the displacement gradient in Y-direction.

Assuming K independent interferograms, the overall likelihood function is written as the product of the likelihood functions for each data set.

$$\begin{aligned} p(\mathbf{d}|\mathbf{m}) &= \Pi_{k=1}^{K} p(\mathbf{d}_k|\mathbf{m}_k) \\ &= \Pi_{k=1}^{K} \big\{ (2\pi)^{-\frac{\sum N_k}{2}} |\mathbf{C}_k|^{-\frac{1}{2}} exp\big[-\tfrac{1}{2}\big(\mathbf{r}_k^T \mathbf{C}_k^{-1} \mathbf{r}_k\big)\big] \big\} \end{aligned} \tag{19}$$

2.2.2 Sampling Approach and Acceptance Rule

Theoretically, Bayesian sampling will produce models from anywhere in the model space, and characterize the posterior PDF according to the probability density. As a result, the sets of models consistent with the prior PDF and the data are sampled more often than those with lower probability (Anderson & Segall, 2013; Minson et al., 2013). Following the Bayesian sampling algorithm provided by GBIS (Bagnardi & Hooper, 2018), we adopt the Monte Carlo Markov Chain (MCMC) algorithm as the probability sampling approach based on the Metropolis-Hastings (MH) rule.

The advantage of MCMC is that it can sample the vector space of the model parameters without specifying their probability density function. In the MCMC sampling algorithm, a random sample moves forward to the next random sample, without dependencies on any samples before the previous one.

$$\mathbf{m}_{i+1} = \mathbf{m}_i + a\Delta\mathbf{m} \tag{20}$$

where a, ranging from -1 to 1, is a random number from a uniform distribution, and $\Delta\mathbf{m}$ is the model step defined in the input file.

The MH rule is thought to be the most important technique for controlling random walk and is able to converge the sampling towards the target distribution (Anderson & Segall, 2013). In MH, the acceptance probability, b, is a random number following the uniform distribution ranging from 0 to 1. If the ratio, $\alpha = p(\mathbf{d}|\mathbf{m}_{i+1})/p(\mathbf{d}|\mathbf{m}_i)$, is higher than b, the new sample $\mathbf{m}_{i+1}$ will be accepted and updated to the new model, and vice versa.

3 Results: Validation Experiments

In section 2, we presented our methodology for constructing a likelihood function between observed and estimated wrapped phase as well as the corresponding variance-covariance matrix, and also the algorithm to generate the samples for the posterior PDF of the estimated model parameters. In this section 3, we validated the performance of our proposed methodology by applying it to two main synthetic case. These exemplify the significant concerns about the most popular volcanic and earthquake ground deformation models.

Table 1. Experiments for Synthetic Case 1

Group	diagonal variance-covariance	block variance-covariance	with wrapped phase	with unwrapped phase
A	√		√	
B		√	√	
C		√		√

3.1 Synthetic Case 1: the effect of likelihood function and noise level

3.1.1 Choice of Likelihood Function

In the likelihood function, the key elements affecting the inversion include the observed data and the weighting matrix. The observed data in conventional InSAR inversion is the unwrapped phase, whereas for our approach it is wrapped. The weighting matrix, which is the inverse of the variance-covariance matrix, describes the noise contained in the observed data. If the weighting matrix is diagonal, it infers that the observation is independent and the spatial correlation among observation is ignored. Hence, the aims of this section are (1) to compare the effect of using observed data by choosing either wrapped or unwrapped phase, and (2) to explore the role of variance-covariance by choosing whether to use diagonal or block variance-covariance.

3.1.2 Experiments Designed with Various Noise Levels

Three groups of experiments were designed: Group A, B and C, as shown in Table 1. The difference between Group A and B is whether spatial correlation is considered in the variance-covariance matrix, and between B and C is whether wrapped or unwrapped phase are used.

In the experiments, patterns of differential interferometric phase change, $\mathbf{\Delta}\phi$, were simulated as the addition of three main components as shown in equation 21, where ϕ_{disp} is the surface displacement phase, ϕ_{atm} is the atmosphere noise phase, and ϕ_{rand} is the random noise phase (e.g. de-correlation and thermal noise).

$$\mathbf{\Delta}\phi = \phi_{disp} + \phi_{atm} + \phi_{rand} \tag{21}$$

Wrapped phase, φ, was calculated by wrapping the differential interferometric phase, $\mathbf{\Delta}\phi$, onto the interval $[-\pi, \pi]$.

$$\varphi = wrap(\mathbf{\Delta}\phi) \tag{22}$$

The displacement phase (ϕ_{disp}) was simulated by using a volcano source (Mogi, 1958) with a spherical shape. The synthetic parameters are listed in Table 2. Figure 3(a) shows the simulated displacement phase. Atmosphere noise phase (ϕ_{atm}) has two physical origins, vertical stratification and turbulent mixing. The vertical stratification is correlated with topography and is temporally more stable. However, the turbulent mixing is governed by strongly non-linear processes, and it is commonly regarded as the most important source of uncertainty in interferograms. Therefore, we generated realistic atmospheric noise phase based on the turbulent mixing in the lower troposphere. Based on the 100×100 km interferograms, Hanssen (2001) studied the tropospheric signal and proposed three scaling regimes between wavenumbers and power spectrum. One regime, where the power spectrum is proportional to the -3/8 power of the wavenumbers, was the most often identified in previous research (Goldstein, 1995; Ferretti et al., 1999). For simplicity, only the regime with a power exponent -8/3 and a scale between 0.25 and 1.5 km was applied in the simulation. Furthermore, we considered three sizes of atmosphere noise phase and explored how well the model parameters could be reconstructed from them. The Signal-to-Atmosphere Noise Ratio, SNR(Atmosphere Noise), is 2, 5, $+\infty$ for the experiment with large, small, or no atmosphere noise phase, which corresponded to the range 50%, 20%, and 0% of the amplitude range of the deformation signal. Figure 3(b) shows a simulated atmosphere noise phase with large magnitude. The random noise phase (ϕ_{rand}) is generally caused by thermal noise in the instrument, and by decorrelation or incoherence (Fattahi, 2015). The random noise in this research was assumed to be spatially uncorrelated white noise, and we contaminated our synthetic data with uniform random noise within the ranges 50%, 20%, and 0% of the amplitude range of the deformation signal. The amplitude range of the deformation signal is with respect to 2π for wrapped phase, or the peak amplitude of displacement phase for the unwrapped phase. The Signal-to-Random Noise Ratio, SNR(Random Noise), is 2, 5, $+\infty$ for the experiments with large, small, or no random noise phase. Figure 3(c) shows an example of a strong decorrelation (random) noise phase component.

Table 2. Source Parameters and Searching Bounds for the Synthetic Case 1 (volcano deformation model)

Parameter Name	Synthetic Value	Starting Value	Searching Bounds	
			Lower	Upper
X center [m]	-1000	-1500	-10000	10000
Y center [m]	-2000	-3000	-10000	10000
Depth [m]	9000	13500	100	10000
Volume Change [m^3]	-3×10^7	-4.5×10^7	-10^9	-10^2

In Figure 4, the simulated noise-plus-deformation wrapped interferogram is shown, as listed in Table 1, and the various noise levels are clearly seen. Then the wrapped phase is downsampled following the algorithm in section 2.1.1. Figures 5(a) and 5(b) show the downsampling results for the case without and with the noise. To estimate the covariance function, we chose an area far from the deformed region and assumed that the phase is dominated by noise, as shown in Figure 6(a). Then we apply the algorithm in section 2.1.2 was applied. For phase gradient, the theoretical semi-variogram function (Figure 6(c)-(d)) was fitted from the downsampled phase gradient (Figure 6(a)-(b)). Note that the downsampled phase gradient was here calculated based on the phase gradient in the patch with uniform size n^2_{thresh}=256.

3.1.3 Evaluation of the Results

After inversion, for each experiment, we assessed the normalised deviation $\mathbf{R}$ of source parameters between the synthetic value $\mathbf{m}$ and the estimated value $\hat{\mathbf{m}}$.

$$\mathbf{R} = \sqrt{\frac{1}{n}\sum_{i=1}^{n}(\frac{\mathbf{m}_i - \hat{\mathbf{m}}_i}{\mathbf{m}_i})^2} \tag{23}$$

where n is the number of source parameters, $\mathbf{m}_i$ is the ith synthetic source parameter value, and $\hat{\mathbf{m}}_i$ is the ith estimated source parameter value. The normalized deviation $\mathbf{R}$ was evaluated from two perspectives: one concerns the source location,

$$\mathbf{R}(location) = \sqrt{\frac{1}{3}\sum_{i=1}^{3}(\frac{\mathbf{m}_i - \hat{\mathbf{m}}_i}{\mathbf{m}_i})^2} \tag{24}$$

where $\mathbf{m} \in$ { X center, Y center, depth }; the other is related to the source strength,

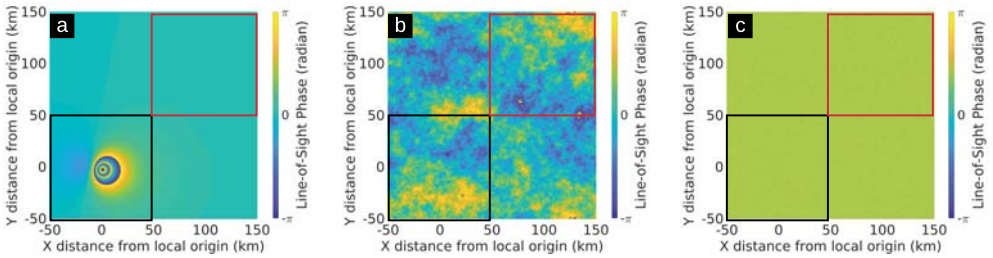

Figure 3. Simulated phase for synthetic case 1 (volcano deformation model). (a) Simulated displacement phase based on a Mogi deformation model (Mogi, 1958). One colored fringe corresponds to one cycle of phase change. (b) Simulated atmosphere noise phase with large magnitude and SNR(Atmosphere Noise)=2, that is, the range of atmosphere noise phase is equivalent to 50% of the amplitude range of the displacement phase. (c) Simulated random noise phase with a large magnitude and SNR(Random Noise)=2, that is, the range of random noise phase is equivalent to 50% of 2π. The area of the region in the black box is around 100km×100km, and this region contains most of the displacement signal, therefore we use this region for phase downsampling. The region in the red box contained few displacement signals and the phase is dominated by the noise phase, so we use it to calculate the covariance function for data weighting.

$$\mathbf{R}(strength) = \sqrt{(\frac{\mathbf{m} - \hat{\mathbf{m}}}{\mathbf{m}})^2} \tag{25}$$

where $\mathbf{m} \in \{$ volume change $\}$.

Under the assumption that the posterior PDF of source parameters follows the normal distribution $\mathcal{N}$, the mean value μ and variance σ^2 were then estimated from normalized deviation $\mathbf{R}$.

$$\mathbf{R} \sim \mathcal{N}(\mu, \sigma^2) \tag{26}$$

Figure 7 shows normalized deviation $\mathbf{R}$ for 3 groups of experiments, where Figure 7(a) is the normalized deviation related to source location, and Figure 7(b) depicts source strength (volume change). We reached some conclusions by comparing results between groups.

(1) Influence of variance-covariance (Group A vs. B): the spatial correlation between patches is not considered to construct the likelihood function in Group A, thus the downsampled patches are independent and have the same weight, while the block variance-covariance considering the spatial correlation is applied to weight the residual

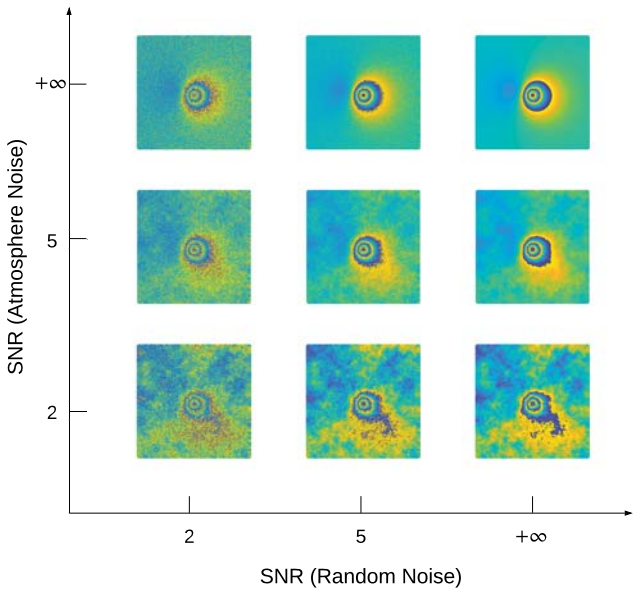

Figure 4. Simulated interferometric wrapped phase in deformed region for Group B in synthetic case 1 (volcano deformation model). The interferometric phase contains the phase that precedes from displacement signal and noise with different levels. The Signal-to-Random Noise Ratio and the Signal-to-Atmosphere Noise Ratio is 2, 5, $+\infty$.

in Group B. For each corresponding experiment, the normalized deviation is greater in Group A where the spatial correlation is neglected.

(2) Influence of observed data (Group B vs. C): the uncertainties of the normalized deviation derived from the wrapped phase (blue distribution) being narrower than that from the unwrapped phase (yellow distribution). Note that the results should be same from both wrapped phase and unwrapped phase without unwrapping error. However, the correlation between circular mean phase and phase gradients or between phase gradients is not considered in WGBIS, and each wrapped dataset is independent, which leads to the underestimated uncertainty.

(3) Influence of atmosphere noise phase (Group B): for experiments using the same SNR(Random Noise) (same column in Figure 7), the mean value of the normalized deviation and the uncertainties became greater with increasing SNR(Atmosphere Noise).

(4) Influence of random noise phase (Group B): for experiments using the same SNR(Atmosphere Noise) (same row in Figure 7), the normalized deviation maintains similar distribution with increasing SNR(Random Noise).

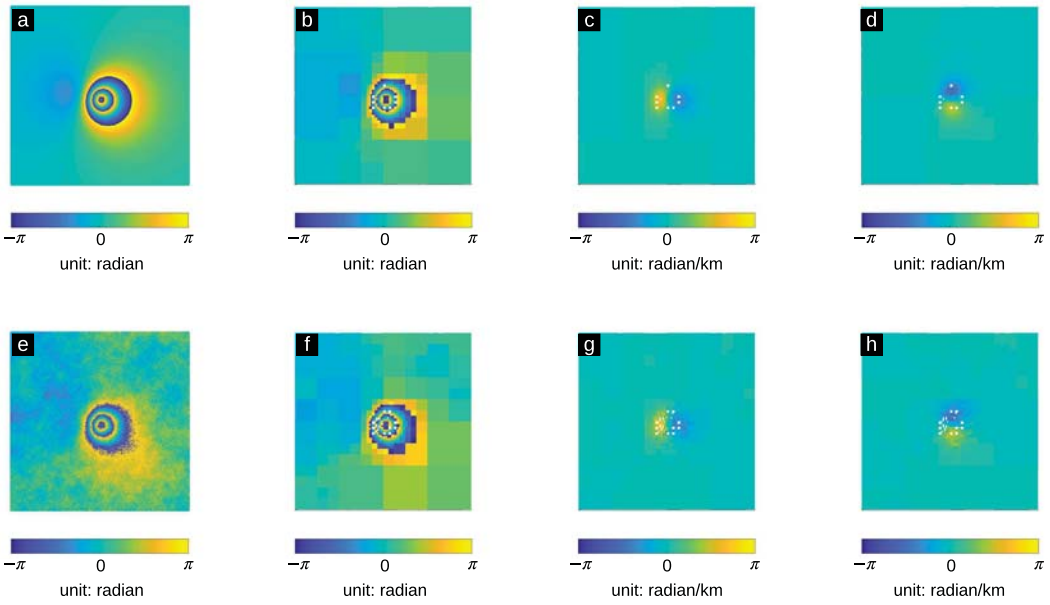

Figure 5. Downsampled wrapped phase in the deformed region for case 1 (volcano deformation model). In the first row, image (a) shows unsampled observed wrapped phase φ in the experiment without noise (top left in Figure 4), while (b)-(d) present its corresponding downsampled circular mean phase $\overline{\varphi}$, phase gradient in X-direction ψ_X and in Y-direction ψ_Y. For the second row (e)-(h), the plotting conventions are same as the first row, but for the experiment containing noise phase (center in Figure 4). The white color in (b)-(d) and (f)-(h) represents patches excluded by the downsampling algorithm.

3.2 Synthetic Case 2: the scenario with strong phase gradient

3.2.1 Strong Phase Gradient Scenario

One situation, where it is difficult to perform inversion is when there is surface rupture with a strong phase gradient, because unwrapping errors are more likely to occur due to the discontinuous phase (Bacques et al., 2018; Shugar et al., 2010). Although the conventional methodology based on the unwrapped phase with unwrapping error might not provide a robust satisfying result in such a scenario, our methodology allows us to explore the inversion results based on the wrapped phase. Therefore, we simulated a fault with surface rupture, and explored the performance with the wrapped and unwrapped phase.

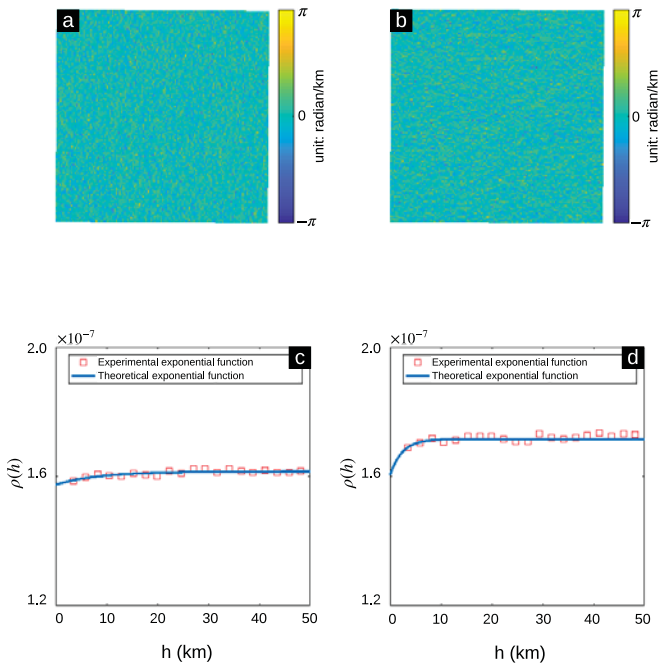

Figure 6. Covariance function estimation from the phase in the non-deformed region for case 1 (volcano deformation model). The chosen region for covariance estimation is the undeformed region for the experiment containing noise phase (the noise level is same as the center figure in 5). Images (a) and (b) are the downsampled phase gradients in X- and Y-directions with minimum pixels n^2_{thresh}=256 as the downsampling threshold. In (c) and (d), the experimental (rectangular) and theoretical (solid line) semivariograms are shown for phase gradients in X- and Y-directions, estimating from (a) and (b) according to equation 9.

3.2.2 Experiments Designed with Strong Phase Gradient

We designed 3 sets of experiments: Groups D, E and F, as shown in Table 3. The difference between Group D and E is that they are either wrapped or unwrapped phase, and between E and F it is whether they contain the unwrapping error. Note that the atmospheric noise and random noise are not considered in these cases. The displacement filed in this case is simulated by half-space fault dislocation model (Okada, 1985) with a major strike slip and minor dip slip. The synthetic parameters are listed in Table 4. Figure 8(a) and Figure 8(c) show the wrapped and unwrapped displacement phase. The maximum slip at surface corresponds to 5∼6 fringes in the line-of-sight direction. An unwrapping error $2\pi k$ in magnitude, where k is an integer, might occur during phase un-

Table 3. Designed Experiments for Synthetic Case 2 (earthquake deformation model)

Group	with wrapped phase	with unwrapped phase	without unwrapping error	with unwrapping error
D	√		√	
E		√	√	
F		√		√

Table 4. Source Parameters and Searching Bounds for Synthetic Case 2 (earthquake deformation model)

Parameter Name	Synthetic Value	Searching Bounds	
		Lower	Upper
Length [m]	8000	5000	40000
Width [m]	6000	1000	30000
Top Depth [m]	10	0	20000
Dip [degree]	88	0	90
Strike [degree]	354	0	360
X center [m]	1000	-5000	5000
Y center [m]	1000	-5000	5000
Strike Slip [m]	0.8	-5.0	5.0
Dip Slip [m]	0.1	-5.0	5.0

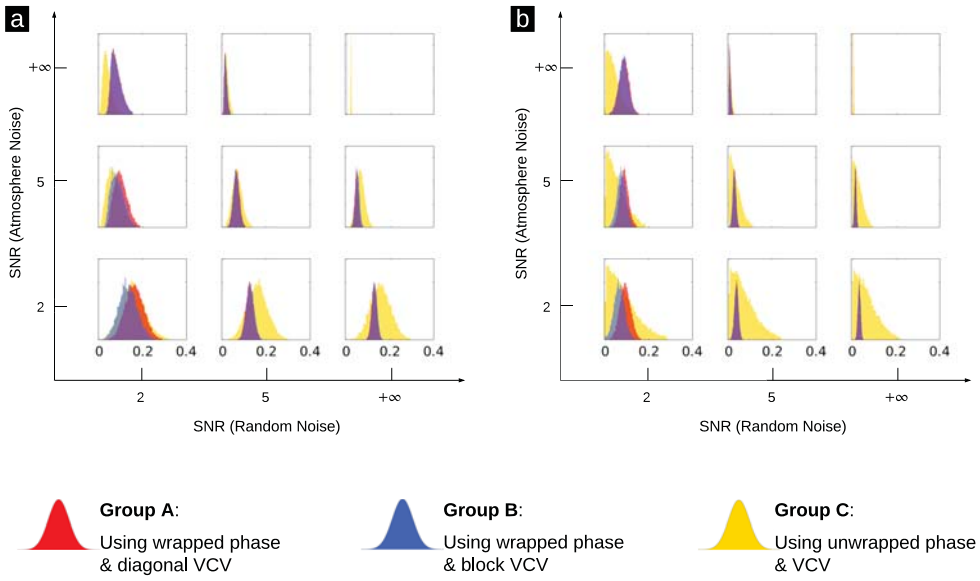

Figure 7. Comparison of inversion results in the volcano case (case 1). Panel (a) is the normalized deviation of location-related parameters. Panel (b) is the normalized deviation of strength-related parameters (volume change). For each panel, the inversion results based on wrapped phase neglecting or considering the off-diagonal variance-covariance term, and unwrapped phase considering variance-covariance are shown as red, blue, and yellow distributions.

wrapping procedure. In this earthquake case, the top depth of the fault plane is as shallow as 10 meters, so it is more likely that unwrapping error would occur. Thus, we assume 4% of downsampled patches to be affected by unwrapping error and k is a random number in {-2,-1,1,2}.

According to Figure 8(a), the total slip at the surface corresponds to 5∼6 fringes in the line-of-sight direction, and 3∼4 of them are identified by the wrapped phase downsampling algorithm with fine details (downsampled circular mean phase in Figure 8(b)). The widths of 2 fringes that fail recognition are less than 10 pixels, and the sharp phase change contributes to a high circular mean deviation of phase, which may contribute to its exclusion. Similarly, the information within the same region is lost in the downsampled unwrapped phase (Figure 8(d)).

435 #### *3.2.3 Evaluation of Results*

436 Following section 3.1.3, the estimated source parameter was assessed by the nor-
437 malized deviation **R** from two perspectives: one is concerned with the location of the sources,
438 and the other with the source strength,

$$\mathbf{R}(strength) = \sqrt{(\frac{\mathbf{m} - \hat{\mathbf{m}}}{\mathbf{m}})^2} \tag{27}$$

439 where $\mathbf{m} \in \{$ geodetic moment $\}$, and geodetic moment is the product of fault length,
440 fault width, total slip, and shear modulus (rigidity). Figure 8(f)-(g) shows normalized
441 deviation **R** for source locations and strength (released moment). Our findings are listed
442 below.

443 (1)If the input data don't contain unwrapping error in either wrapped phase or un-
444 wrapped phase without unwrapping error, the methodology provided good inversion re-
445 sults. However, the mean value and uncertainty of normalized deviation based on the
446 wrapped phase (blue distribution) was slightly lower than that based on the unwrapped
447 phase (yellow distribution).As mentioned in section 3.1.3, the results should be the same
448 either from wrapped phase or unwrapped phase without unwrapping error, and the un-
449 derestimated uncertainty for wrapped phase is because each wrapped dataset is inde-
450 pendent.

451 (2) If the input data is the unwrapped phase, the addition of unwrapping error will
452 corrupt the inversion result. The normalised deviation (black distribution) exceeded 0.6
453 when adding 4% of unwrapping error.

454 4 Discussion

455 4.1 Choice of the Likelihood Function

456 The key in this Bayesian inversion methodology is the new likelihood function in
457 which the residual between observed and modeled wrapped phase is weighted by the variance-
458 covariance matrix. In this section, we will discuss the effect on the method's performance
459 of the choice of observed wrapped phase and variance-covariance matrix.

460 In previous inversion methodologies based on the wrapped phase, the input data
461 is limited to one observable. For example, Feigl and Thurber (2009) minimized the cir-
462 cular mean deviation based on the wrapped phase, and Ali and Feigl (2012) minimized
463 that based on the phase gradient in Y-direction. In order to show the effect of input data

on the inversion results, we used our Bayesian approach to design a set of experiments with different input data: (a) circular mean phase, (b) phase gradient in Y-direction, and (c) combinations of circular mean phase and phase gradients. These experiments suggest that the mean value of the normalized deviation based on the circular mean phase (a) is lower than that based on their combinations (c). In contrast, the inversion with only circular mean phase (a) is easily trapped into a local minimum due to a wrong estimation of integer k. We also noticed that the mean value of the normalized deviation based on the circular mean phase (a), is higher than that based on their combinations (c), and that the uncertainties based on the phase gradient (b) are 1∼6 times wider than those based on their combinations (c). It can therefore be concluded that the inversion based on the combinations provides a more appropriate estimation for the source parameters.

As shown in Figure 7, for experiments based on wrapped phase and variance-covariance matrix considering the correlation between pixels (Group B), the uncertainty of normalized deviation is lower than that based on unwrapped phase (Group C). Unlike the independent observations among different interferograms, the three downsampled wrapped phases are not fully independent, explained by the change in the wrapped phase being correlated with that in phase gradient. Thus, the ignorance of the correlation between circular mean phase and phase gradients, or between phase gradients, would lead to an excessive fit with the observed data and underestimated uncertainties (Fukuda & Johnson, 2008; Sun et al., 2013; Bekaert et al., 2016). Moreover, the difference between uncertainties based on wrapped and unwrapped phase decreased when the noise level rose. This infers that, under high noise conditions, the inversion based on wrapped phase could lead to a similar uncertainty of the model, compared with that based on unwrapped phase. Nevertheless, it would be better to apply an appropriate algorithm to estimate the correlation between the three downsampled wrapped phases, and this needs further exploration.

4.2 Effect of Noise on Results

4.2.1 Effect of Increase in Random Noise Phase

In this research, the random noise phase is simulated as spatially uncorrelated white noise (a decorrelated effect), and the experiment in section 3.1 presents the inversion re-

sult with various noise levels. When comparing the experiments with the same atmosphere noise, using the proposed approach, the PDFs of the normalized deviation remain stable under various random noise levels (Figure 10).

In order to explore the performance of the proposed approach under extreme noise conditions, we broadened the extent of the simulated random noise level. Noise levels are expressed as SNR(Random Noise) ranging from 1, 1.1, ..., 10, $+\infty$. This corresponds to the percentage of random noise phase with respect to 2π for wrapped phase cases, or the peak amplitude of the deformation phase for unwrapped phase cases, 100%, 90%, ..., 10%, 0%. Although the data with such low SNR(Random Noise), e.g. 1 or 1.1, may not exist in the real case, it is still valuable to test the limits of our approach.

In order to explore the effect of random noise phase, we plot the inversion results versus random noise levels. Figure 10 shows the mean value of the normalized deviation of source parameters with SNR(Random Noise) in horizontal direction. In Figure 10(a)-(b), the inversion with wrapped phase stays robust with increasing random noise level. In comparison to the Bayesian inversion with unwrapped phase, the mean values of R(location) and R(strength) based on wrapped phase are lower, as shown in Figure 10(a) and (c) (or Figure 10(b) and (d)). It is also notable that the inversion with the unwrapped phase still had a good performance when SNR(Random Noise)=1.2, assuming no unwrapping error. In reality, unwrapping errors might occur when SNR reaches such a low value, where random noise dominates the interferometric phase, and performance will be severely influenced. Therefore, the good performance when inverted by unwrapped phase with SNR(Random Noise)=1.2 as input data is an ideal but unattainable case.

4.2.2 Effect of Increase in Atmosphere Noise Phase

Atmosphere noise has been widely regarded as the most difficult error to mitigate in surface deformation detection, because both signals are long-wavelength and are not easy to separate. Although many methods have been developed to diminish the effect of atmosphere noise for the unwrapped phase, such as the topography-dependent method (Elliott et al., 2008) and the external data-based method (Jolivet et al., 2014), a general methodology applicable to all conditions is still under discussion (Bekaert et al., 2016; Yu et al., 2018). In section 3.1, our analysis inferred that the normalised deviation of location and strength would be biased up to 0.08 with SNR(Atmosphere Noise)=2. Sim-

ilarly, Scott and Lohman (2016) demonstrated the biased fault parameters due to the impact of atmosphere noise.

In order to explore the performance of our approach under extremely strong atmosphere phase, we broadened the extent of simulated random noise level and the SNR(Atmosphere Noise) ranged from 1, 1.1, ..., 10, $+\infty$. This corresponds to the percentage range of atmosphere noise phase to the peak amplitude of the deformation phase, 100%, 90%, ..., 10%, 0%.

In Figure 10(a)-(b), for inversion with the wrapped phase, the mean value of normalized deviation distribution decreased quasi-linearly with increasing SNR(Atmosphere Noise). For inversion with the unwrapped phase in Figure 10(c)-(d), a linear relationship is still applicable. Another significant feature is the uncertainty of the distribution, which is 5 times wider than with wrapped phase on average, and it also decreases with decreasing SNR(Atmosphere Noise).

4.3 Exploring the Limits of the Search in the Parameter Space Using Wrapped Phase

4.3.1 Effect of Strong Phase Gradient

In order to reduce the number of observations and also the influence of noise phase, several algorithms have been proposed to downsample the unwrapped phase (Jonsson et al., 2002; Simons et al., 2002; Lohman & Simons, 2005). In this paper, we proposed a new methodology to downsample the wrapped phase. For the case with low phase gradient, our algorithm provided good downsampled patches describing the deformation signal under SNR low to 1.2. However, it would be more difficult to downsample the wrapped phase with a high gradient, since the interferometric fringes are so closely spaced that aliasing occurs. In this case, the estimated gradient would be too low in absolute value. Therefore, the choice of downsampling criteria, such as circular mean deviation and minimum pixels in one patch, is critical to generate good downsampling results. (1) The circular mean deviation affects to what extent the deformation signal could be detected. If the circular mean deviation threshold is over-estimated, the fringe we prefer to keep could be lost and the deformation signal would be ignored. (2) The threshold of minimum pixels in one patch decides in which details the fringe pattern could be detected. If we double the threshold of the minimum pixels, the deformation signal would be av-

eraged. For the region with high phase gradient, the width of the fringe is narrow and the over-estimated minimum pixels threshold will lead to the exclusion of the displacement signal. Thus, the initial minimum pixels threshold could be low and then adjusted to a suitable value according to the noise level and the pattern of deformation signal. (3) The necessary condition for interferometry implies the maximum detectable deformation gradient is one fringe per pixel (Massonnet & Feigl, 1998), but, in real data, phase gradients in excess of this threshold seem to be fairly rare. Strong tilts and rotations can cause the phase gradient to exceed this limit (Peltzer et al., 1994).

4.3.2 Effects of Searching Bounds and Starting Models

In order to find the global minimum of an objective function for nonlinear equations, global optimization algorithms, e.g., Bayesian approach (Amey et al., 2018; Bagnardi & Hooper, 2018) and the simulated annealing algorithm (Cervelli et al., 2001; Jonsson et al., 2002), are widely used for geophysical problems, due to their high efficiency and capability of jumping out of local minimum regions of a high-dimensional parameter space. One concern about WGBIS is whether it could be caught in a sub-optimal solution. The initialization procedure for these global optimization algorithms consists of two steps, to: (1) set bounds on the values for all the model parameters and (2) pick an initial starting model. We therefore set out to test the performance of WGBIS under various of starting models and searching bounds. The starting model is 0%, 10%, or 100% off the synthetic value, and the searching bound of volume change is in a narrow or wide range. The results revealed that WGBIS could retrieve the input model values with a normalized deviation as low as 0.01 in all cases.

In comparison, the program embedded with the simulated annealing algorithm, General Inversion for Phase Technique (GIPhT) (Feigl & Thurber, 2009; Ali & Feigl, 2012), is also applied to invert for the optimal model. The input phase is either circular mean phase (Feigl & Thurber, 2009) or phase gradient in X-rection (Ali & Feigl, 2012). The same starting model and searching bounds are set as mentioned above. The experiments revealed the following findings. (1) With phase gradient in X-direction as input data, GIPhT successfully finds the global minimum with normalized deviation as low as 0.01. (2) With circular mean phase as input data, GIPhT failed in one case, where the range of searching bounds is wide and the starting model is strongly biased (100%) away from the synthetic value. As demonstrated by Shirzaei and Walter (2009), the success of sim-

ulated annealing at finding a global solution critically depends on the cooling schedule. This is substantially problemdependent, so it seems impracticable to develop a global remedy for all problems.

4.4 Exploring the Performance in a Real Case

In order to test the performance of this methodology with actual data, we investigated the surface deformation caused by the 2019 Acipayam earthquake in Turkey. This M_w 5.7 earthquake based on published focal mechanisms was generated by a normal fault. This is consistent with the regional tectonics in southwestern Turkey, which are dominated by extensional stresses. We computed a descending interferogram using the European Space Agency's Sentinel-1 satellite images in Terrain Observation by Progressive Scans (TOPS) mode from 11/03/2019 to 23/03/2019. This period spans the occurrence of the earthquake and should be dominated by any co-seismic displacement. The area shows very good coherence, and a clear strong fringe pattern is visible (Figure 11(a)). The interferogram was computed using the JPL/Caltech/Stanford ISCE package, and was spatially filtered.

The filtered interferometric phase pattern was fed directly into WGBIS, which downsampled the wrapped phase and phase gradients data, estimated the data variance-covariance matrix, and finally ran the Bayesian inversion for the fault rupture parameters. Figure 11(b) shows the downsampled observed wrapped phase and phase gradients, modeled phase, and their residuals. In Figure 12(a), we also show very well-defined posterior PDFs for the nine estimated fault source parameters. The bottom row shows the histograms of marginal distributions for each parameter and the remaining rows showing the joint distributions between pairs of parameters. In Figure 12(b), we show that the distributions of parameters in the prior have significantly narrowed down to the posterior distribution after the Bayesian inversion.

The Bayesian inversion results reveal that co-seismic surface displacement can be well explained by fault slip on a 9.4±0.2-km-long and 9.2±0.2-km-wide fault, striking 340°±1.2° and shallowly dipping at 29.3°±1.5°, with 14±0.5 cm of slip in the down-dip direction and 7±1 cm of sinistral strike-slip components. The estimated fault slip infers that this fault has a dominate extensional mechanism with minor left lateral strike-slip component, and this is consistent with geologic and geomorphologic investigation (rem

Table 5. Prior and Posterior Source Parameters for 2019 Acipayam Earthquake

Parameter Name	Searching Bounds (Prior)		Posterior
	Lower	Upper	
Length [m]	6000	12000	9400±200
Width [m]	6000	10000	9200±200
Top Depth [m]	0	8000	3500±130
Dip [degree]	20	80	29.3±1.5
Strike [degree]	0	360	340±1.2
X center [m]	-20000	20000	6600±240
Y center [m]	-20000	20000	2200±130
Strike Slip [m]	-0.5	0.5	0.07±0.01
Dip Slip [m]	-2	2	-0.14±0.005

Elitez & Yaltrak, 2016). From the analysis of the marginal posterior probabilities (Figure 12(a)), correlations are observed between any two of the source parameters, with all of them reasonably well-defined. Assuming a shear modulus of $3.32\times10^{10}N/m^2$, Poisson's ratio 0.25 and the marginal posterior probabilities for fault geometry and slip, the geodetic moment is $4.45\pm0.2\times10^{17}Nm$, equivalent to M_w between 5.68 and 5.71. This finding is consistent with the estimated seismic moment M_w 5.7 from the available earthquake catalogs (Turkey earthquake catalog, `http://www.koeri.boun.edu.tr/sismo/2/earthquake-catalog/`; GFZ earthquake catalog, `https://geofon.gfz-potsdam.de/old/eqinfo/list.php`; USGS earthquake catalog, `https://earthquake.usgs.gov/earthquakes/search/`). It should also be pointed out that, during the Bayesian inversion, the searching bounds for the fault parameters were selected over quite a broad range, e.g., the striking angle is searched between 0° and 360° (see Table 5 for more details). This indicates that our methodology has the ability to distinguish two conjugate fault planes inferred from the seismic wave inversion. However, this could be due to the very shallow fault slip associated with this event. Furthermore, a strong indicator that our estimated fault plane is the causative slipping fault, is that the spatial distribution of aftershocks is closely aligned to the modeled fault plane (Figure 13).

5 Conclusions

This research has developed a new methodology for estimating earthquake and volcano source parameters, by inverting the interferometric wrapped phase using a customized Bayesian approach. We firstly introduce a new downsampling algorithm suitable for the wrapped phase, and another algorithm to estimate the variance-covariance matrix for describing the noise contained in the wrapped phase. Then, we propose a new likelihood function for the observed and modeled wrapped phase. Finally, a Bayesian approach is applied to generate the probability distribution function (PDF) of the likelihood function, which is proportional to the posterior PDF of the source model by assuming a uniform PDF. Benefiting from the proposed methodology, the advantages are demonstrated by the simulated experiments and are listed as follows.

(1) The wrapped phase is directly used in our inversion methodology, so the concerns about the unwrapping error are no longer worrisome. An improved downsampling algorithm provides a fine observed data for the inversion.

(2) Embedded with a Bayesian approach, the methodology provides an assessment of the model uncertainty and it also has the capability to escape the local minimum.

(3) The block variance-covariance describing the noise contained in the wrapped phase is considered in the likelihood function, thus providing an optimistic source model, better than that used when neglecting the off-diagonal variance-covariance term.

(4) The robustness of our methodology was validated with multiple likelihood functions, in simulated cases with various noise levels, in a scenario with strong phase gradients, and in an actual earthquake case by using real SAR datasets.

(5) In terms of its performance with respect to noise, the range of application for WGBIS is extended compared with that for GBIS (Figure 14).

In future, this new method could be a complementary inversion method applied in volcano and fault source parameters estimation, and contribute to solving the long-standing problem of inversion with unwrapped phase due to unwrapping error.

Acknowledgments

This research was supported by a Chinese Scholarship Council - University of Liverpool joint scholarship awarded to Yu Jiang (201706450071). This research was partially funded by the NERC project Centre for the Observation and Modelling of Earthquakes, Volcanoes and Tectonics (COMET, GA/13/M/031, http://comet.nerc.ac.uk). Copernicus

SAR data are retrieved from scihub.copernicus.eu. The SAR image on March 11 2019 is retrieved from https://scihub.copernicus.eu/dhus/odata/v1/Products('a0e79b65-d206-4e43-b962-c832045d05df')/$value, with identifier `S1A_IW_SLC__1SDV_20190311T040709_20190311T040736_026285_02F00C_6A73`. The SAR image on March 23 2019 is retrieved from https://scihub.copernicus.eu/dhus/odata/v1/Products('4af832c6-9549-45c6-9f33-2fb497141b5b')/$value, with identifier `S1A_IW_SLC__1SDV_20190323T040709_20190323T040736_026460_02F67D_EC68`. Sentinel-1 interferograms in the paper can be downloaded from Zenodo (http://doi.org/10.5281/zenodo.xxxxxx). The WGBIS software can be downloaded from Zenodo (http://doi.org/10.5281/zenodo.xxxxxx) together with its user manual and sample synthetic data. The authors are also grateful to Valérie Cayol, John Elliott, Sam Wimpenny, and Zhenhong Li for insightful discussions of different aspects of this manuscript, as well as to two anonymous reviewers, Editor Paul Tregoning and Associate Editor Andy Hooper for their helpful and constructive reviews, which greatly improved this manuscript. The authors thank Guido Jones for proofreading and improving the quality of the English.

References

Ali, S. T., & Feigl, K. L. (2012). A new strategy for estimating geophysical parameters from InSAR data: Application to the Krafla central volcano in Iceland. *Geochemistry, Geophysics, Geosystems*, *13*(6). doi: 10.1029/2012GC004112

Amey, R. M. J., Hooper, A., & Walters, R. J. (2018). A Bayesian method for incorporating self-similarity into earthquake slip inversions. *Journal of Geophysical Research: Solid Earth*, *123*(7), 6052–6071. doi: 10.1029/2017JB015316

Anderson, K., & Segall, P. (2013). Bayesian inversion of data from effusive volcanic eruptions using physics-based models: Application to Mount St. Helens 2004-2008. *Journal of Geophysical Research: Solid Earth*, *118*(5), 2017–2037. doi: 10.1002/jgrb.50169

Bacques, G., de Michele, M., Raucoules, D., Aochi, H., & Rolandone, F. (2018). Shallow deformation of the San Andreas fault 5 years following the 2004 Parkfield earthquake (Mw6) combining ERS2 and Envisat InSAR. *Scientific Reports*, *8*(1), 6032. doi: 10.1038/s41598-018-24447-3

Bagnardi, M., & Hooper, A. (2018). Inversion of surface deformation data for rapid estimates of source parameters and uncertainties: A Bayesian ap-

proach. *Geochemistry, Geophysics, Geosystems*, *19*(7), 2194–2211. doi: 10.1029/2018GC007585

Bekaert, D. P. S., Segall, P., Wright, T. J., & Hooper, A. J. (2016). A network inversion filter combining GNSS and InSAR for tectonic slip modeling. *Journal of Geophysical Research: Solid Earth*, *121*(3), 2069–2086. doi: 10.1002/2015JB012638

Biggs, J., Wright, T., Lu, Z., & Parsons, B. (2007). Multi-interferogram method for measuring interseismic deformation: Denali Fault, Alaska. *Geophysical Journal International*, *170*(3), 1165–1179. doi: 10.1111/j.1365-246X.2007.03415.x

Cervelli, P., Murray, M. H., Segall, P., Aoki, Y., & Kato, T. (2001). Estimating source parameters from deformation data, with an application to the March 1997 earthquake swarm off the Izu Peninsula, Japan. *Journal of Geophysical Research: Solid Earth*, *106*(B6), 11217–11237. doi: 10.1029/2000JB900399

Chen, C. W., & Zebker, H. A. (2001). Two-dimensional phase unwrapping with use of statistical models for cost functions in nonlinear optimization. *Journal of the Optical Society of America A*, *18*(2), 338. doi: 10.1364/JOSAA.18.000338

Costantini, M. (1998). A novel phase unwrapping method based on network programming. *IEEE Transactions on Geoscience and Remote Sensing*, *36*(3), 813–821. doi: 10.1109/36.673674

Elliott, J. R., Biggs, J., Parsons, B., & Wright, T. J. (2008). InSAR slip rate determination on the Altyn Tagh Fault, northern Tibet, in the presence of topographically correlated atmospheric delays. *Geophysical Research Letters*, *35*(12). doi: 10.1029/2008GL033659

Fattahi, H. (2015). *Geodetic imaging of tectonic deformation with insar* (Doctoral dissertation). Retrieved from `https://scholarlyrepository.miami.edu/oa_dissertations/1456`

Feigl, K. L., & Sobol, P. E. (2013). PHA2QLS.C: A computer program to compress images of wrapped phase by simultaneously estimating gradients and quadtree resampling.
doi: https://github.com/feigl/gipht/blob/master/pha2qls/pha2qls.c

Feigl, K. L., & Thurber, C. H. (2009). A method for modelling radar interferograms without phase unwrapping: Application to the M 5 Fawnskin, California earthquake of 1992 December 4. *Geophysical Journal International*, *176*(2),

491–504. doi: 10.1111/j.1365-246X.2008.03881.x

Ferretti, A., Prati, C., & Rocca, F. (1999, March). Multibaseline InSAR DEM reconstruction: the wavelet approach. *IEEE Transactions on Geoscience and Remote Sensing*, *37*(2), 705-715. doi: 10.1109/36.752187

Flynn, T. J. (1997). Two-dimensional phase unwrapping with minimum weighted discontinuity. *Journal of the Optical Society of America A*, *14*(10), 2692. doi: 10.1364/JOSAA.14.002692

Fornaro, G., Atzori, S., Calo, F., Reale, D., & Salvi, S. (2012). Inversion of wrapped differential interferometric SAR data for fault dislocation modeling. *IEEE Transactions on Geoscience and Remote Sensing*, *50*(6), 2175–2184. doi: 10.1109/TGRS.2011.2173584

Fukuda, J., & Johnson, K. M. (2008). A fully Bayesian inversion for spatial distribution of fault slip with objective smoothing. *Bulletin of the Seismological Society of America*, *98*(3), 1128–1146. doi: 10.1785/0120070194

Galetto, F., Hooper, A., Bagnardi, M., & Acocella, V. (2020). The 2008 eruptive unrest at Cerro Azul volcano (Galpagos) revealed by InSAR data and a novel method for geodetic modelling. *Journal of Geophysical Research: Solid Earth*, *125*(2), e2019JB018521. doi: 10.1029/2019JB018521

Goldstein, R. M. (1995). Atmospheric limitations to repeat-track radar interferometry. *Geophysical Research Letters*, *22*(18), 2517-2520. doi: 10.1029/95GL02475

Goldstein, R. M., Zebker, H. A., & Werner, C. L. (1988). Satellite radar interferometry: Two-dimensional phase unwrapping. *Radio Science*, *23*(4), 713–720. doi: 10.1029/RS023i004p00713

Gombert, B., Duputel, Z., Jolivet, R., Doubre, C., Rivera, L., & Simons, M. (2018). Revisiting the 1992 Landers earthquake: A Bayesian exploration of co-seismic slip and off-fault damage. *Geophysical Journal International*, *212*(2), 839–852. doi: 10.1093/gji/ggx455

González, P. J., Bagnardi, M., Hooper, A. J., Larsen, Y., Marinkovic, P., Samsonov, S. V., & Wright, T. J. (2015). The 2014-2015 eruption of Fogo volcano: Geodetic modeling of Sentinel-1 TOPS interferometry. *Geophysical Research Letters*, *42*(21), 9239–9246. doi: 10.1002/2015GL066003

González, P. J., & Fernández, J. (2011). Error estimation in multitemporal InSAR deformation time series, with application to Lanzarote, Canary Islands. *Journal of Geophysical Research*, *116*(B10), B10404. doi: 10.1029/2011JB008412

Hanssen, R. F. (2001). *Radar interferometry* (Vol. 2). Dordrecht: Springer Netherlands. doi: 10.1007/0-306-47633-9

Hooper, A. (2010). Bayesian inversion of wrapped InSAR data for geophysical parameter estimation. In *ESA Living Planet Symposium.* ESA Communications.

Huang, M.-H., Fielding, E. J., Liang, C., Milillo, P., Bekaert, D., Dreger, D., & Salzer, J. (2017). Coseismic deformation and triggered landslides of the 2016 Mw 6.2 Amatrice earthquake in Italy. *Geophysical Research Letters*, *44*(3), 1266–1274. doi: 10.1002/2016GL071687

Hussain, E., Hooper, A., Wright, T. J., Walters, R. J., & Bekaert, D. P. S. (2016). Interseismic strain accumulation across the central North Anatolian Fault from iteratively unwrapped InSAR measurements. *Journal of Geophysical Research: Solid Earth*, *121*(12), 9000–9019. doi: 10.1002/2016JB013108

Jammalamadaka, S. R., & SenGupta, A. (2001). *Topics in circular statistics.* World Scientific. doi: 10.1142/4031

Jolivet, R., Agram, P. S., Lin, N. Y., Simons, M., Doin, M.-P., Peltzer, G., & Li, Z. (2014). Improving InSAR geodesy using global atmospheric models. *Journal of Geophysical Research: Solid Earth*, *119*(3), 2324–2341. doi: 10.1002/2013JB010588

Jonsson, S., Zebker, H., Segall, P., & Amelung, F. (2002). Fault slip distribution of the 1999 Mw 7.1 Hector Mine, California, earthquake, estimated from satellite radar and GPS measurements. *Bulletin of the Seismological Society of America*, *92*(4), 1377–1389. doi: 10.1785/0120000922

Kent, J. (1978). Limiting behaviour of the von mises-fisher distribution. *Mathematical Proceedings of the Cambridge Philosophical Society*, *84*(3), 531536. doi: 10.1017/S030500410005533X

Lohman, R. B., & Simons, M. (2005). Some thoughts on the use of InSAR data to constrain models of surface deformation: Noise structure and data downsampling. *Geochemistry, Geophysics, Geosystems*, *6*(1). doi: 10.1029/2004GC000841

Mardia, K. V., & Jupp, P. E. (2000). *Directional statistics.* J. Wiley.

Mardia, K. V., & Voss, J. (2014). Some fundamental properties of a multivariate von Mises distribution. *Communications in Statistics - Theory and Methods*, *43*(6), 1132-1144. doi: 10.1080/03610926.2012.670353

Massonnet, D., & Feigl, K. L. (1998). Radar interferometry and its application to changes in the earth's surface. *Reviews of Geophysics*, *36*(4), 441-500. doi: 10.1029/97RG03139

Minson, S. E., Simons, M., & Beck, J. L. (2013). Bayesian inversion for finite fault earthquake source models I-theory and algorithm. *Geophysical Journal International*, *194*(3), 1701–1726. doi: 10.1093/gji/ggt180

Mogi, K. (1958). Relationship between eruptions of various volcanoes and the deformation of the ground surfaces around them. *Bulletin of the Earthquake Research Institute*, *36*, 99–134.

Nikolaidis, N., & Pitas, I. (1998). Nonlinear processing and analysis of angular signals. *IEEE Transactions on Signal Processing*, *46*(12), 3181–3194. doi: 10.1109/78.735295

Nodehi, A., Golalizadeh, M., Maadooliat, M., & Agostinelli, C. (2018). Estimation of multivariate wrapped models for data in Torus. Retrieved from `https://arxiv.org/abs/1811.06007`

Okada, Y. (1985). Surface deformation due to shear and tensile faults in a half-space. *Bulletin of the Seismological Society of America*, *75*(4), 1135–1154.

Peltzer, G., Hudnut, K. W., & Feigl, K. L. (1994). Analysis of coseismic surface displacement gradients using radar interferometry: new insights into the landers earthquake. *Journal of Geophysical Research: Solid Earth*, *99*(B11), 21971-21981. doi: 10.1029/94JB01888

Pepe, A. (2019). Theory and statistical description of the enhanced multi-temporal insar (e-mtinsar) noise-filtering algorithm. *Remote Sensing*, *11*(3). doi: 10.3390/rs11030363

Ragon, T., Sladen, A., & Simons, M. (2018). Accounting for uncertain fault geometry in earthquake source inversions I: theory and simplified application. *Geophysical Journal International*, *214*(2), 1174–1190. doi: 10.1093/gji/ggy187

Sandwell, D. T., & Price, E. J. (1998). Phase gradient approach to stacking interferograms. *Journal of Geophysical Research: Solid Earth*, *103*(B12), 30183–30204. doi: 10.1029/1998JB900008

Scott, C. P., & Lohman, R. B. (2016). Sensitivity of earthquake source inversions to atmospheric noise and corrections of InSAR data. *Journal of Geophysical Research: Solid Earth*, *121*(5), 4031–4044. doi: 10.1002/2016JB012969

Shirzaei, M., & Walter, T. R. (2009). Randomly iterated search and statistical competency as powerful inversion tools for deformation source modeling: Application to volcano interferometric synthetic aperture radar data. *Journal of Geophysical Research*, *114*(B10), B10401. doi: 10.1029/2008JB006071

Shugar, D. H., Rabus, B. T., & Clague, J. J. (2010). Elevation changes (1949-1995) of Black Rapids Glacier, Alaska, derived from a multi-baseline InSAR DEM and historical maps. *Journal of Glaciology*, *56*(198), 625–634. doi: 10.3189/002214310793146278

Simons, M., Fialko, Y., & Rivera, L. (2002). Coseismic deformation from the 1999 Mw 7.1 Hector Mine, California, earthquake as inferred from InSAR and GPS observations. *Bulletin of the Seismological Society of America*, *92*(4), 1390–1402. doi: 10.1785/0120000933

Sun, J., Shen, Z.-K., Bürgmann, R., Wang, M., Chen, L., & Xu, X. (2013). A three-step maximum a posteriori probability method for InSAR data inversion of coseismic rupture with application to the 14 April 2010 Mw 6.9 Yushu, China, earthquake. *Journal of Geophysical Research: Solid Earth*, *118*(8), 4599–4627. doi: 10.1002/jgrb.50244

Vasyura-Bathke, H., Dutta, R., Jónsson, S., & Mai, M. (2017). A new Bayesian earthquake analysis tool (BEAT). In *EGU* (Vol. 19, p. 9318).

Wang, C., Ding, X., & Li, Q. (2014). Coseismic slip inversion based on InSAR arc measurements. *Natural Hazards and Earth System Sciences*, *14*(3), 649–656. doi: 10.5194/nhess-14-649-2014

Werner, C. L., Wegmuller, U., Strozzi, T., Wegmüller, U., & Strozzi, T. (2002). *Processing strategies for phase unwrapping for insar applications.* VDE-Verlag.

Whipple, K. X., Shirzaei, M., Hodges, K. V., & Ramon Arrowsmith, J. (2016). Active shortening within the Himalayan orogenic wedge implied by the 2015 Gorkha earthquake. *Nature Geoscience*, *9*(9), 711–716. doi: 10.1038/ngeo2797

Xu, W., & Cumming, I. (1996). A region growing algorithm for InSAR phase unwrapping. In *IGARSS '96. 1996 International Geoscience and Remote Sens-*

ing Symposium (Vol. 4, pp. 2044–2046). IEEE. doi: 10.1109/IGARSS.1996.516883

Yu, C., Li, Z., Penna, N. T., & Crippa, P. (2018). Generic atmospheric correction model for interferometric synthetic aperture radar observations. *Journal of Geophysical Research: Solid Earth*, *123*(10), 9202–9222. doi: 10.1029/2017JB015305

rem Elitez, & Yaltrak, C. (2016). Miocene to Quaternary tectonostratigraphic evolution of the middle section of the Burdur-Fethiye Shear Zone, south-western Turkey: Implications for the wide inter-plate shear zones. *Tectonophysics*, *690*, 336 - 354. doi: 10.1016/j.tecto.2016.10.003

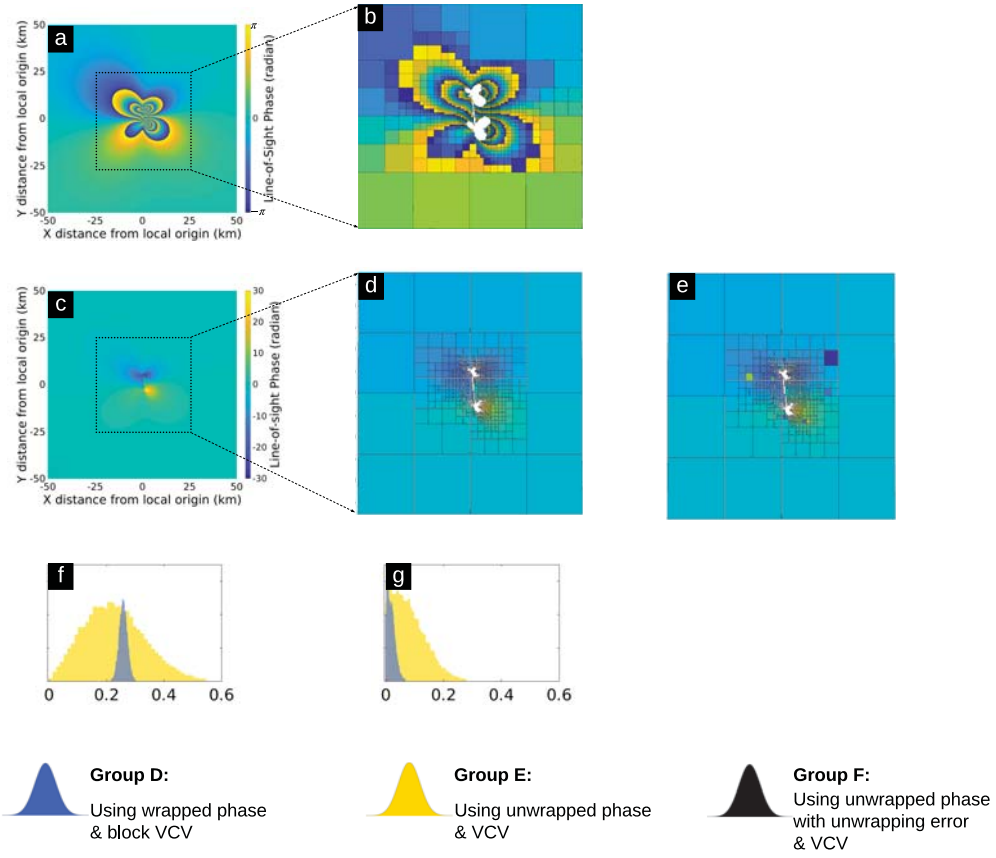

Figure 8. Simulated interferometric phase in case 2 (earthquake deformation model) and the comparison of inversion results. Panel (a) is the simulated wrapped phase, and (b) is the downsampled circular mean phase in the region with the dotted line. Panel (c) is the simulated unwrapped phase, and (d) is the downsampled unwrapped phase. The downsampling threshold for (e) is the same as (d), but we assume 4% of the downsampled patches contain the unwrapping error, $2\pi k$, where k is a random integer in {-2,-1,1,2}. The white color in (b), (d), (e) represents patches excluded by the downsampling algorithm. The bottom row is the inversion result by using (b), (d), (e) as the input data, and (f) and (g) is the normalized deviation of location- and strength-related parameters. For each panel, the inversion results based on wrapped phase and unwrapped phase without and with unwrapping error are shown as blue, yellow, and black distributions. There is no black distribution in (f) and (g) since their normalized deviation exceeds 0.6.

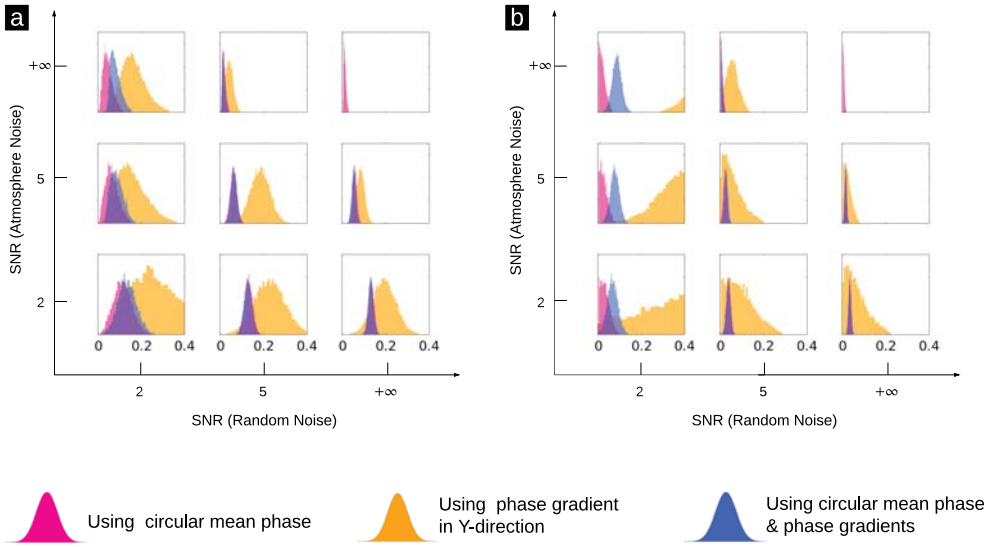

Figure 9. Comparison of inversion results in the volcano case (section 4.1). Panel (a) is the normalized deviation of location-related parameters. Panel (b) is the normalized deviation of strength-related parameters (volume change). For each panel, the inversion results based on circular mean phase, phase gradient in Y-direction and their combinations are shown as pink, orange, and blue distributions.

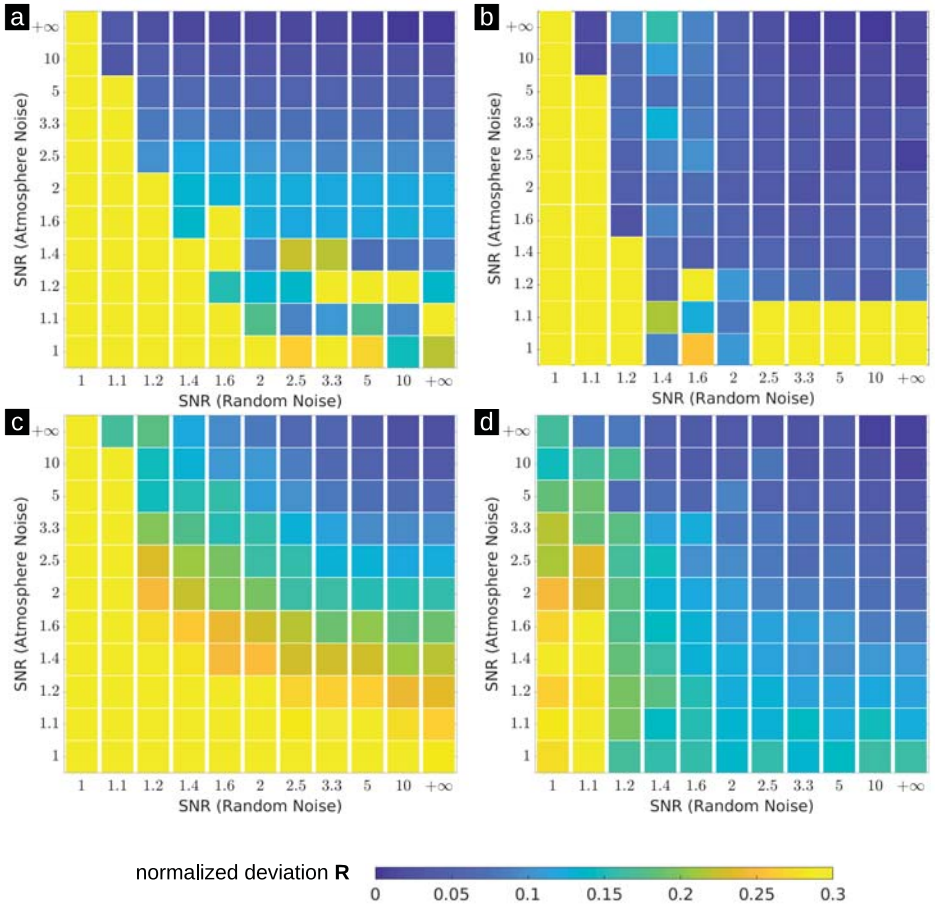

Figure 10. The inversion results with input data under various noise levels. The first row shows the inversion results based on the wrapped phase, and panels (a)&(b) show the mean value of normalized deviation in terms of source location- and strength-related parameters. The plotting conventions of the second row are the same as the first row, but based on the unwrapped phase.

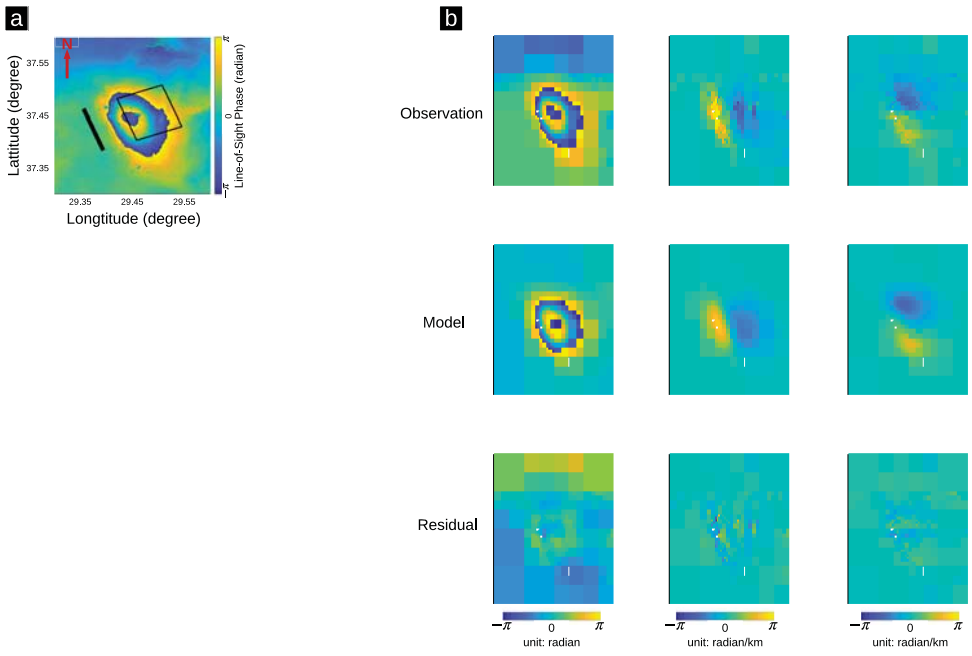

Figure 11. Observation and inversion results for 2019 Acipayam earthquake (Turkey). Image (a) is the observed wrapped phase of the interferogram (reference image acquisition date: 11/03/2019; secondary image acquisition date: 23/03/2019). Image (b) shows the observed, modeled and residual wrapped phase, and the wrapped phase from left to right is circular mean phase, and phase gradient in X- and Y-direction. The black rectangle in (a) shows the surface projection of the model with maximum likelihood, and the black line is the fault plane extended to the surface.

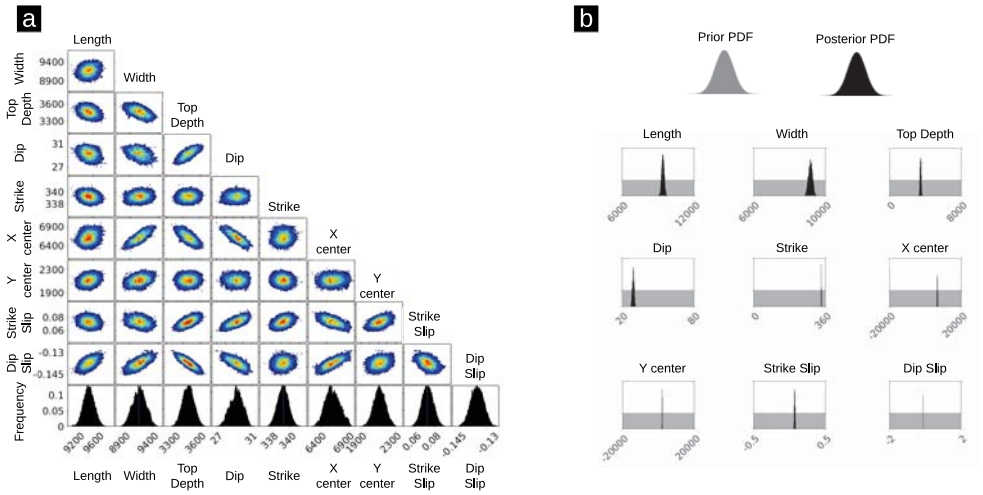

Figure 12. Posterior and prior PDFs for the fault source parameters in 2019 Acipayam earthquake (Turkey). (a) shows the posterior PDFs for the fault source parameters: the bottom rows show the histograms of marginal distributions for each parameter and the remaining rows the joint distributions between pairs of parameters. X center and Y center in (a) refer to the coordinates of the middle point of the bottom line of the fault plane relative to point [29.45°N, 37.45°E]. (b) shows the comparison between prior assumption (gray color) and posterior estimation(black color). The posterior PDF in (b) shows same distributions with those in the bottom row in (a).

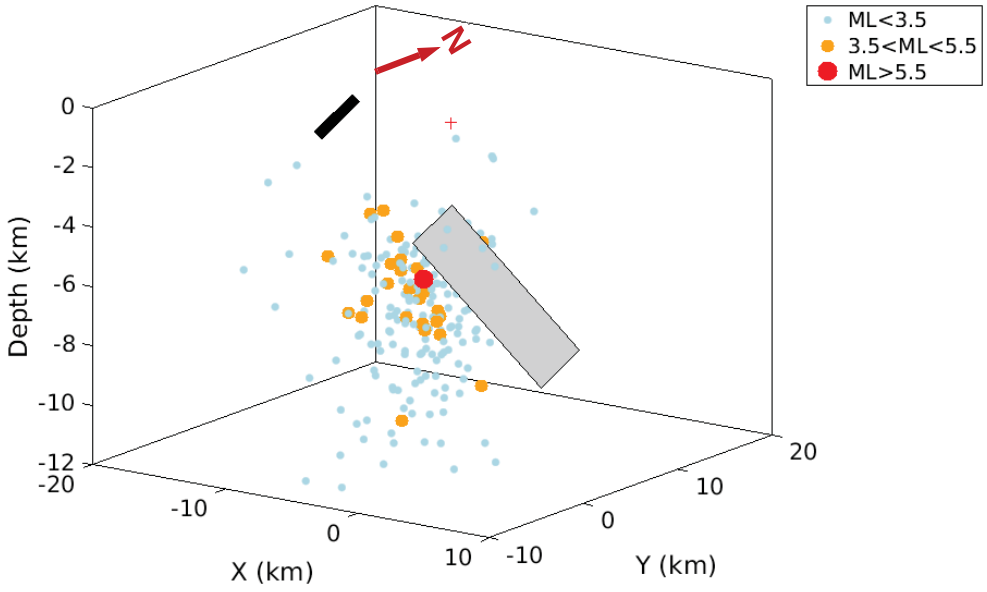

Figure 13. Modeled fault slip and distribution of earthquakes during 2019 Acipayam earthquake sequence. The gray rectangle is the inverted fault plane based on the model with maximum likelihood, and the black line is the fault plane extended to the surface. The red dot marks the location for the main shock epicenter. The red cross marks the reference point [29.45°N, 37.45°E]. The orange and blue dots are aftershocks with ML>3.5 and ML<3.5 in the first month following the main shock, retrieved from Turkey earthquake catalog: `http://www.koeri.boun.edu.tr/sismo/2/earthquake-catalog/`.

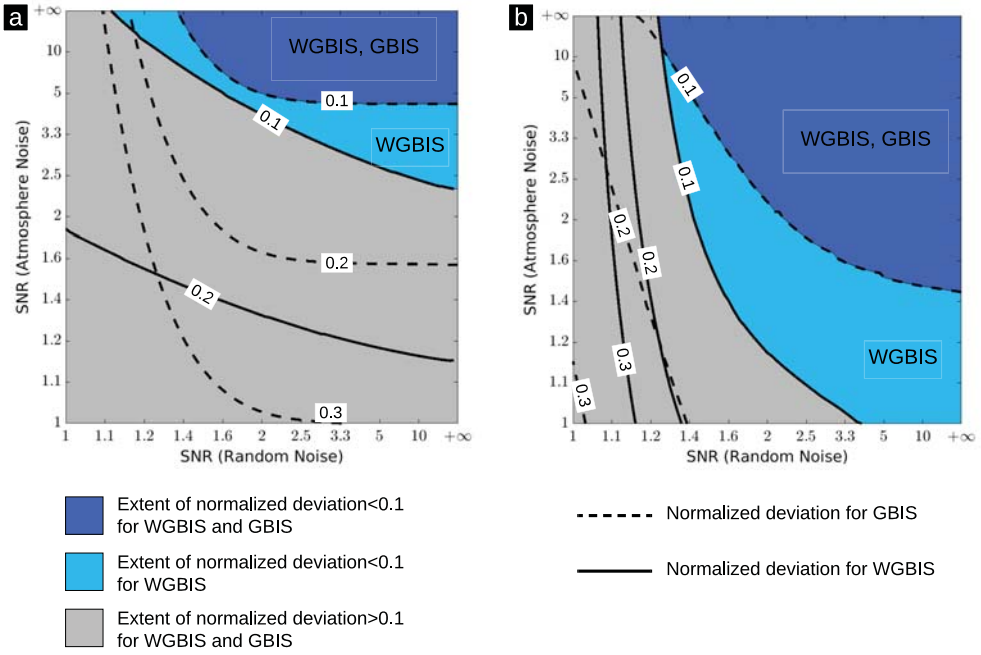

Figure 14. The extent of application for WGBIS and GBIS in terms of noise level. Panel (a) and (b) show the application extent calculated on the basis of normalized deviation of source location- and strength-related parameters. The black line is the experimental function fitting the normalized deviation in Figure 10 and the fitted function is $\mathbf{R} = q_1 x^{-q_2} + q_3 y^{-q_4} + q_5 x^{-1} y^{-1} + q_6$, where $\mathbf{R}$ is the normalized deviation, x is SNR(Random Noise), y is SNR(Atmosphere Noise), and q is function coefficient. The solid line is the normalized deviation for WGBIS, and dashed line for GBIS. The dark blue region is the common extent where normalized deviation is lower than 0.1 for both WGBIS and GBIS. The light blue region is the extended application extent for WGBIS. The gray region stands for normalized deviations higher than 0.1 for both WGBIS and GBIS.